

GEOPHYSICS

Slab temperature controls on the Tonga double seismic zone and slab mantle dehydration

S. Shawn Wei,^{1,2*} Douglas A. Wiens,¹ Peter E. van Keken,³ Chen Cai¹

Double seismic zones are two-layered distributions of intermediate-depth earthquakes that provide insight into the thermomechanical state of subducting slabs. We present new precise hypocenters of intermediate-depth earthquakes in the Tonga subduction zone obtained using data from local island-based, ocean-bottom, and global seismographs. The results show a downdip compressional upper plane and a downdip tensional lower plane with a separation of about 30 km. The double seismic zone in Tonga extends to a depth of about 300 km, deeper than in any other subduction system. This is due to the lower slab temperatures resulting from faster subduction, as indicated by a global trend toward deeper double seismic zones in colder slabs. In addition, a line of high seismicity in the upper plane is observed at a depth of 160 to 280 km, which shallows southward as the convergence rate decreases. Thermal modeling shows that the earthquakes in this “seismic belt” occur at various pressures but at a nearly constant temperature, highlighting the important role of temperature in triggering intermediate-depth earthquakes. This seismic belt may correspond to regions where the subducting mantle first reaches a temperature of ~500°C, implying that metamorphic dehydration of mantle minerals in the slab provides water to enhance faulting.

INTRODUCTION

Intermediate-depth earthquakes, which occur at depths of ~70 to 300 km, are observed at most subduction zones. The causes for this seismicity remain controversial because the pressure (P) and temperature (T) are too high to allow brittle failure. Of particular interest are double seismic zones (DSZs) discovered in several subduction zones, in which intermediate-depth earthquakes occur along two layers that are parallel to the subducting slab and are separated by 20 to 40 km (1–10). The upper plane is usually confined in the slab crust and uppermost mantle with downdip compressional stresses, whereas the lower plane is deeper in the slab mantle with downdip tensional stresses.

A variety of mechanisms have been proposed to explain these earthquakes, including dehydration embrittlement (11), plastic shear instability (12), transformational faulting (6), and fluid-related embrittlement (13). The upper zone hypocenters coincide well with locations where free fluids can be produced by dehydration reactions. This suggests that intermediate-depth earthquakes may be triggered by increased pore fluid pressure that reduces the confining pressure at great depths. The free fluids are usually assumed to be derived from in situ dehydration of hydrous minerals (14–16) or by migration from elsewhere (17).

The Tonga subduction zone is a particularly interesting place to study intermediate-depth seismicity because it represents the coldest slab, due to the subduction of old oceanic lithosphere with the largest convergence velocity of any subduction zone. Thus, temperature-controlled processes, such as most dehydration reactions, should occur at greater pressures and depths than those observed in other subduction zones. The convergence rate decreases southward from ~240 mm/year at 16°S to ~164 mm/year at 22°S (Fig. 1) (18), whereas the slab age and dip angle roughly remain constant. The DSZ in Tonga was initially discovered using global seismic data by Kawakatsu (2), with an estimated depth range from 60 to 200 km. Although the slab is dominated by downdip compressional stresses (19), the few earthquakes in the lower plane of the DSZ are characterized by downdip tensional stresses (2, 20).

¹Department of Earth and Planetary Sciences, Washington University, St. Louis, MO 63130, USA. ²Institute of Geophysics and Planetary Physics, Scripps Institution of Oceanography, University of California, San Diego, La Jolla, CA 92093, USA. ³Department of Terrestrial Magnetism, Carnegie Institution for Science, Washington, DC 20015, USA.

*Corresponding author. Email: shawnwei@ucsd.edu

2017 © The Authors, some rights reserved; exclusive licensee American Association for the Advancement of Science. Distributed under a Creative Commons Attribution NonCommercial License 4.0 (CC BY-NC).

Because of the lack of local seismic data, Tonga earthquake hypocenters listed in all standard global earthquake catalogs, such as the *EHB Bulletin* (21), generally have large uncertainties. Therefore, the Tonga DSZ has not been precisely delineated, and the regional connection between intermediate-depth seismicity and slab processes, such as dehydration reactions, remains unclear. Here, we present precise hypocenters of 671 intermediate-depth earthquakes in the Tonga subduction zone (Fig. 1 and fig. S1) using data from local island-based, ocean-bottom, and global seismographs (fig. S2), which provide an unprecedented image of the Tonga DSZ. Among these earthquakes, 324 have Global Centroid Moment Tensor (CMT) solutions (22, 23), allowing us to determine the stress state within the slab (figs. S3 to S5).

RESULTS

The detailed seismicity cross sections show a DSZ in the northern and central parts of the study area (Fig. 2). The existence of the DSZ is further demonstrated by plotting the number of earthquakes as a function of the depth normal to the slab surface along each cross section (Fig. 3A). In the northernmost region (A-A'), where there are few local seismic stations, the hypocenters do not show a clear double-planed structure, but the focal mechanisms appear to be separated with downdip compressional events closer to the slab surface and downdip tensional ones deeper within the slab. This is in agreement with results from Kawakatsu (2, 20), who proposed the existence of the DSZ largely based on focal mechanisms. Along cross sections B-B', C-C', and D-D', the lower plane of the DSZ can be identified simply on the basis of the distribution of the slab-normal depths (Fig. 3A). In the south, the lower plane diminishes, and the seismogenic zone becomes a single layer of downdip compressional earthquakes along cross section E-E' (Fig. 2E). The only downdip tensional event in the south is the earthquake on 22 June 1977 ($M_W = 8.2$), at a depth of 61 km in the Global CMT catalog and 85 km in this relocation (E-E' in fig. S5). Its unusually large magnitude, relatively shallow depth, and location seaward of the usual DSZ position suggest that it is not a regular DSZ lower-plane earthquake and may be related to the subduction of the Louisville Ridge (24). Neither the slab surface nor the DSZ can be explicitly determined by the standard global earthquake compilations such as the *EHB Bulletin* (21) without local seismic data (fig. S1B).

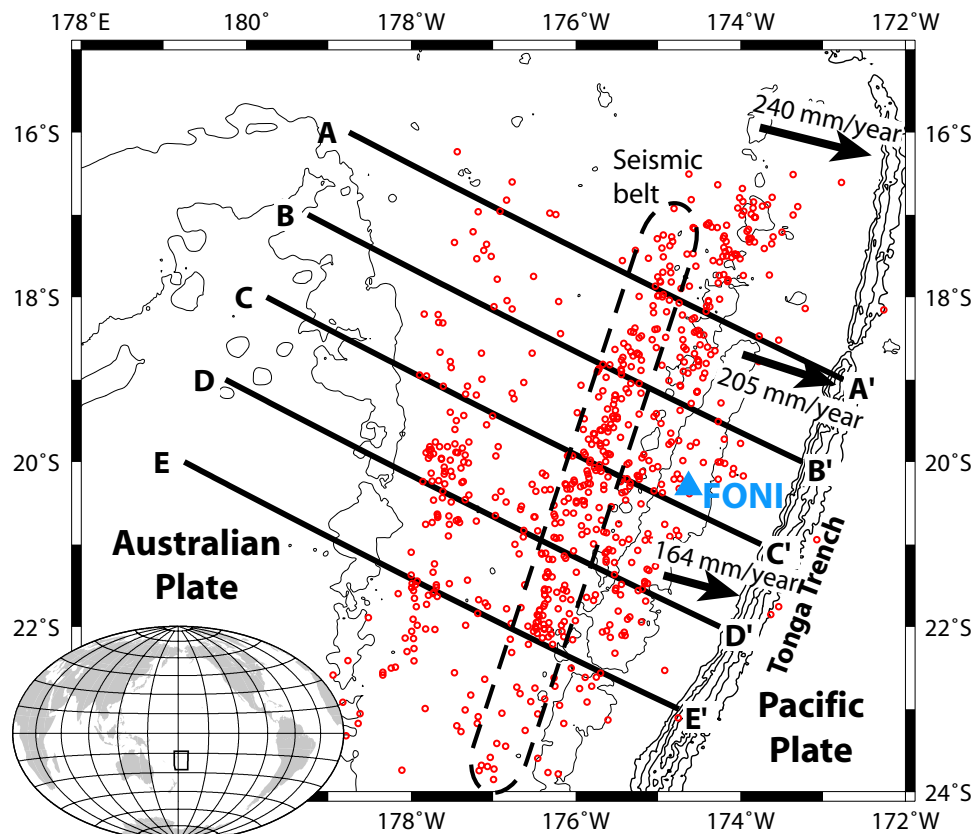


Fig. 1. Map of relocated epicenters (red circles). Straight lines indicate the cross sections with a width of 133 km in this study. Earthquake depths range from 50 to 450 km. Dashed rectangle highlights the seismic belt discussed in the main text. Black arrows with numbers show the Global Positioning System site velocities in a Pacific-fixed reference frame (18). Blue triangle represents station FON1 in Fig. 4. Bathymetry of a depth of 1 km is contoured to outline the Tonga Ridge, Tofua Arc, Lau Ridge, and Fiji Plateau, and contours of 7, 8, 9, and 10 km are also shown to delineate the Tonga Trench. Inset displays the study region in a global map.

The best earthquake locations, providing the highest-resolution DSZ image, are those located using both local and global stations along cross section C-C', beneath the center of the 2009–2010 array (Fig. 4 and fig. S6). Because most of these earthquakes are relatively small compared to those with CMT solutions, the waveforms have lower signal-to-noise ratios and limited bandwidth; thus, it is difficult to determine reliable focal mechanisms. The analysis of waveform similarity suggests that the seismogenic zone along C-C' can be roughly divided into two layers, so that most of the upper-layer events are similar to an upper-plane earthquake with a downdip compressional CMT mechanism, whereas the waveforms from lower-plane events resemble those from a downdip tensional CMT earthquake (Fig. 4).

The delineation of the two seismic planes is not as clear as observed for the DSZ in northeastern Japan [for example, see study by Kita et al. (8)], but this may not indicate a difference in the separation of the two planes. Tonga event locations are less accurate than for northeastern Japan, and in particular, those events that are solely constrained by global stations (black dots in fig. S6) have larger uncertainties and may cause the DSZ to be less distinct. Perhaps more importantly, the lower plane of the Tonga DSZ is significantly less active compared to that of the northeastern Japan DSZ, making it more difficult to identify the two distinct planes. It is intriguing that the absence of the DSZ lower plane in the south coincides with a change in the deeper slab geometry, going from a torn or contorted slab in the northern and central parts (25) to a continuous slab in the south. The slab stress state also becomes

strongly compressional in the south over all depth ranges (19, 26). Therefore, we suggest that the change in the overall slab stress field is responsible for the absence of the DSZ in south Tonga.

Our new results show that the DSZ in Tonga extends to a depth of ~300 km (Figs. 3B and 4 and fig. S6), which is significantly deeper than what was found by Kawakatsu (2, 20). It also extends significantly deeper than DSZs in other subduction zones, which we interpret as resulting from the colder slab temperature due to the higher convergence rate. Following Kirby *et al.* (11), we describe the slab temperature using the thermal parameter, defined as the product of plate age and the vertical descent rate of the slab. The thermal parameter is proportional to the depth to which an isotherm will extend in the mantle assuming only conductive heat transfer. Figure 5 shows a strong correlation between the depth extent of the DSZ within various subduction zones (3–9) and the thermal parameters given by Syracuse and Abers (27), suggesting that the termination of the DSZ is predominantly controlled by slab temperature. This demonstrates that the fundamental controls on maximum DSZ depth result from thermally activated processes, such as slab dehydration, and not from purely geometric factors related to slab bending, which varies among subduction zones.

The highest Tonga intermediate-depth seismicity rate occurs along a linear pattern of epicenters at about a depth of 280 km in the north, shallowing to 160 km in the south, labeled as the “seismic belt” in Figs. 1 and 2. This belt appears as an earthquake cluster along each cross section, as illustrated by histograms of event depths in fig. S7.

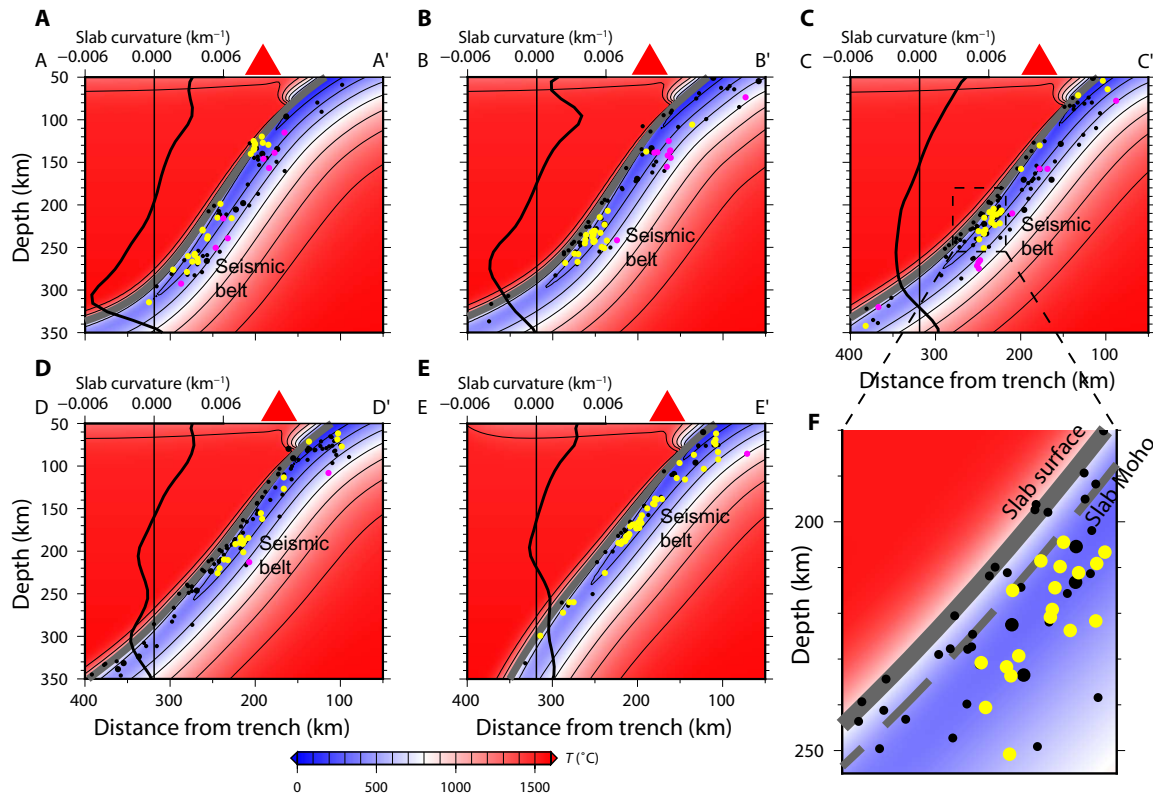


Fig. 2. Cross sections of hypocenters superposed on thermal models. (A to E) Hypocenters with thermal models for each cross section. The temperature contour interval is 200°C. The gray curve shows the slab surface fit to the seismicity, and the red triangle on the top represents the volcanic arc. Earthquakes are sorted into the categories of downdip compression (yellow dots), downdip tension (magenta dots), and null (black dots) on the basis of the directions of the principal axes shown in fig. S5. Small black dots illustrate the events without a CMT solution. Superposed on the left is the slab curvature along each cross section. (F) Enlarged view of cross section C-C' to show the seismic belt. Yellow and black dots are the actual hypocenters. The solid and dashed gray curves illustrate the slab surface and Moho, respectively.

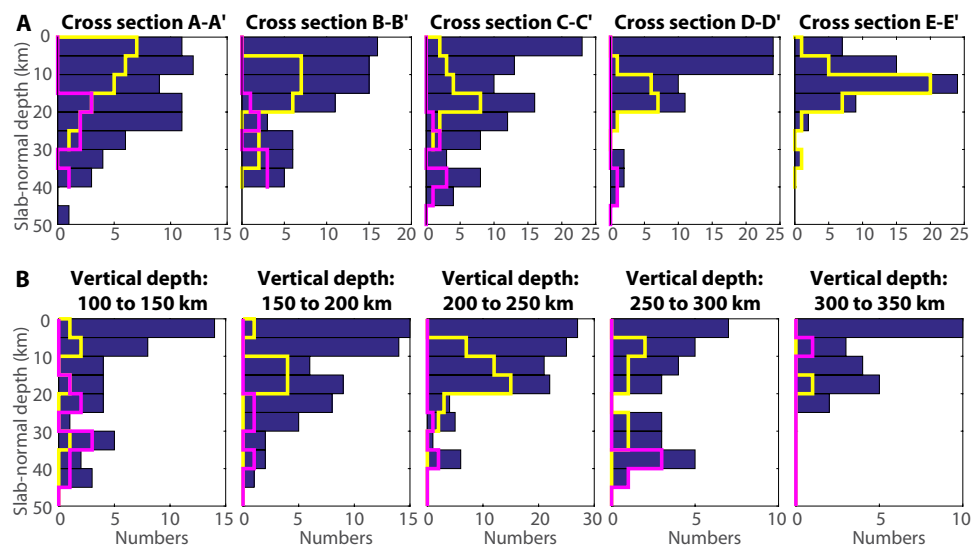


Fig. 3. Histograms of earthquake depths below the slab surface in the slab-normal direction. (A) Earthquakes at vertical depths of 100 to 300 km along each cross section. Downdip compressional and tensional events are shown in yellow and magenta, respectively. In the south, the seismogenic zone becomes a single layer of downdip compressional earthquakes along cross section E-E'. (B) All earthquakes along cross sections B-B', C-C', and D-D' sorted into five subsets according to their vertical depths. The DSZ lower plane disappears below the vertical depth of ~300 km.

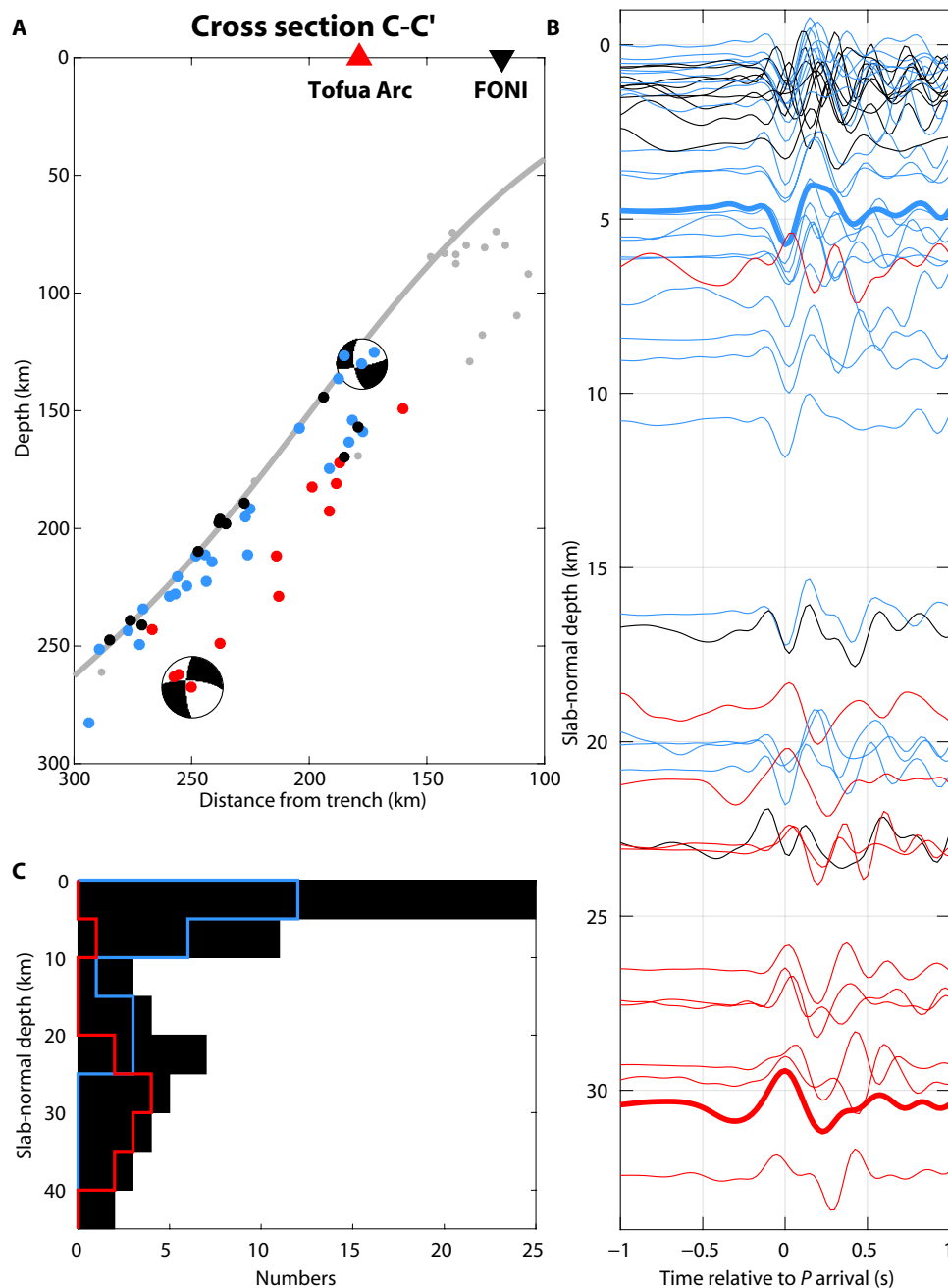


Fig. 4. Waveform similarity analysis along cross section C-C'. (A) Locations for events recorded by both global stations and the 2009–2010 local deployment. Two of the events have CMT solutions, with the upper plane event showing downdip compression and the lower plane event showing downdip tension. Gray curve shows the slab surface fit by the seismicity, and the red triangle on the top represents the volcanic arc. We compare waveforms of these events recorded at station FONI in Tonga (black triangle), because the raypaths are roughly parallel with the slab. Events right beneath FONI [gray dots in (A)] are excluded to avoid near-vertical raypaths. Blue, red, and black dots indicate three groups of earthquakes sorted in (B). (B) Seismograms recorded at FONI filtered at 1 to 5 Hz. The bold blue waveform shows the seismogram of the downdip compressional earthquake near the slab surface, whereas the seismogram of the downdip tensional event is shown with a bold red curve. These two waveforms are shifted so that the peak amplitudes are aligned to 0 s. Seismograms of other events are aligned on the basis of waveform cross-correlation. All events are sorted into three groups according to their cross-correlation coefficients: blue events similar to the downdip compressional CMT event, red events similar to the downdip tensional CMT event, and black events that show ambiguous similarities. (C) Histogram of all earthquake depths in the slab-normal direction (black). Blue and red histograms correspond to the blue and red events sorted in (B), respectively.

Some other earthquake clusters, such as the one at a depth of 125 to 150 km along cross sections A-A' and B-B', do not extend for long distances along strike (map view in Fig. 1 and 3D view in fig. S8). We thus focus our investigations on the seismic belt at a depth of 160 to 280 km. It is unlikely that these earthquakes are caused by the change

in the slab geometry, because the slab curvature changes at greater depths (Fig. 2 and fig. S7). A similar seismic belt in the upper plane of the DSZ has also been observed in northeastern Japan and has been attributed to the formation of eclogite within the slab crust (28). Kita *et al.* (28) further proposed that the deepening of the seismic belt

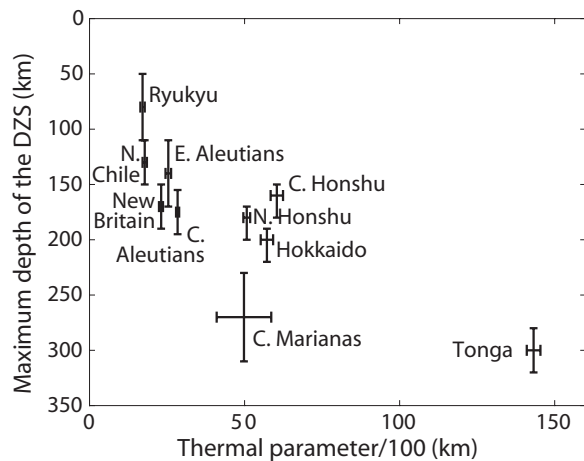


Fig. 5. Depth of the maximum downward extent of the DSZ versus thermal parameter for different subduction zones. The thermal parameter is defined as the product of plate age, convergence velocity, and the sine of the slab dip angle, and it is proportional to the depth at which a given isotherm would be subducted (11). Thermal parameters are given by Syracuse *et al.* (48), except for Mariana, which shows rapid lateral variations in thermal parameter along strike. In this case, we calculated the thermal parameter for 18°N, where the DSZ is observed (9). The maximum depth of the Tonga DSZ is quantitatively estimated on the basis of histograms in Fig. 3B. The maximum DSZ depths in other subduction zones are visually estimated on the basis of previous studies for eastern Aleutians (4), New Britain (5), Ryukyu trench (6), northern Chile (7), central Marianas (9), and northeastern Japan (8).

beneath the Hokkaido corner results from a change in the slab temperature and emphasized the predominant role of thermally controlled mechanisms. By comparison, the seismic belt in Tonga occurs at greater depths. Because the convergence rate decreases almost linearly from north to south (18), whereas slab age and dip angle are constant, the slab interior temperature must increase linearly from north to south, coinciding with the trend that the seismic belt occurs at shallower depths toward the south.

The strong correlation between the depth extent of the DSZs and the slab thermal parameter, combined with the correlation between the depth of the seismic belt and the convergence rate, suggests that one or more thermally controlled mechanisms are responsible for the DSZ and the seismic belt. To quantify these effects, we developed two-dimensional (2D) thermal models for each cross section, taking into account the varying slab geometry and convergence rate. The other parameters, including the plate age and sediment thickness, are constant for all cross sections (see tables S1 and S2). The differences between the 2D cross sections are therefore primarily due to the varying slab geometry and the convergence rate. As expected, the cold core of the Tonga slab extends deeper in the north than in the south and also deeper compared to that in northeastern Japan (13) and other slabs because of the high convergence rate in Tonga.

From these thermal models (Fig. 2, A to E), we extract the P - T conditions of the slab surface and earthquakes along each cross section (Fig. 6, A to E). We also assumed a slab crustal thickness of 5.5 km on the basis of a previous active-source seismic study of the incoming Pacific Plate (29) to determine the P - T conditions of the Moho. The seismic belt is quantitatively defined as the peak of seismic activity in both pressure and temperature shown in fig. S9. Figure 6F shows that the P - T conditions of the seismic belt earthquakes along all the cross sections are within a narrow thermal range of 325° to 425°C, despite a wide pressure range of 4.5 to 8.5 GPa. Most of these earthquakes are located at the Moho or within the uppermost mantle of the subducting

slab (Fig. 2F), and CMT solutions and waveform similarity analysis, which indicate downdip compression, associate them with the DSZ upper plane. This suggests that the seismic belt occurs where the upper plane, likely confined to the crust at shallower levels by comparison to Japan (28), descends into the subducting mantle. This suggests that a temperature-activated process in the uppermost subducting mantle is responsible for the seismic belt. However, the temperature in the earthquake foci is highly uncertain because of possible systematic errors introduced by fitting the slab surface to the hypocenters. Given the strong thermal gradients near the slab surface, relatively small errors in slab surface or hypocenter location can translate into large differences in predicted temperature. The estimated errors of pressure are negligible, but the thermal uncertainties can be as large as 300°C for earthquakes near the slab surface (Fig. 6, A to E).

More precise estimates of the controlling temperatures may be obtained if we assume that the seismic belt occurs where the mantle immediately beneath the Moho is heated above some threshold. The thermal structure of the slab Moho is more robust because it primarily depends on the thickness of the subducting oceanic crust, which is well resolved by previous seismic refraction studies (29). Plots of the Moho temperature adjacent to the seismic belt hypocenters (Fig. 5F) show that the P - T conditions of the Moho are restricted in an even narrower temperature range of 475° to 525°C. Therefore, both the actual P - T conditions calculated for the earthquakes and the P - T conditions of the adjacent Moho show nearly isothermal trends.

DISCUSSION

Our study indicates a strong correlation between DSZ depth extents and slab thermal conditions (Fig. 5). In addition, thermal modeling shows nearly isothermal trends for the seismic belt earthquakes and the adjacent Moho (Fig. 6F). These observations suggest that the Tonga DSZ is controlled by one or several temperature-sensitive mechanisms rather than slab geometry or pressure. Although several possible mechanisms are temperature-controlled, we suggest that serpentine dehydration reactions are the most plausible candidates because of the widespread occurrence of serpentine in the subducting mantle and because serpentine dehydration is expected at the temperature and pressure conditions where the seismicity is observed [for example, see study by Hacker *et al.* (15)].

The P - T conditions of the subducting uppermost mantle in the southern and central regions of the seismic belt are 5.5 to 7 GPa and 500°C, respectively, and correspond closely with the first dehydration reaction of antigorite (antigorite = phase A + enstatite + H₂O) along the Moho geotherm (Fig. 6) (30–32). Therefore, we suggest that the seismic belt earthquakes are triggered by water released from antigorite dehydration in the uppermost mantle immediately beneath the Moho. This is consistent with a conclusion by Brudzinski *et al.* (10), who compared DSZ layer separations and slab ages worldwide. Many studies indicate that seawater reacts with mantle peridotite to form serpentine minerals (including antigorite) in plate bending faults on the incoming plate just seaward of trenches (33–36), and that antigorite will be the dominant hydrous mineral in the subducting mantle. Some of the seismic belt earthquakes may occur closer to the Moho than they appear in Fig. 2 because of the large uncertainties of those hypocenters constrained solely by global data. However, some earthquakes occurring at colder temperatures 10 to 15 km below the Moho (Fig. 2F) are still plausible, because a few numerical models show that pressure gradients within the slab may drive the water deeper into the slab (17, 37) and cause seismicity by fluid-related embrittlement.

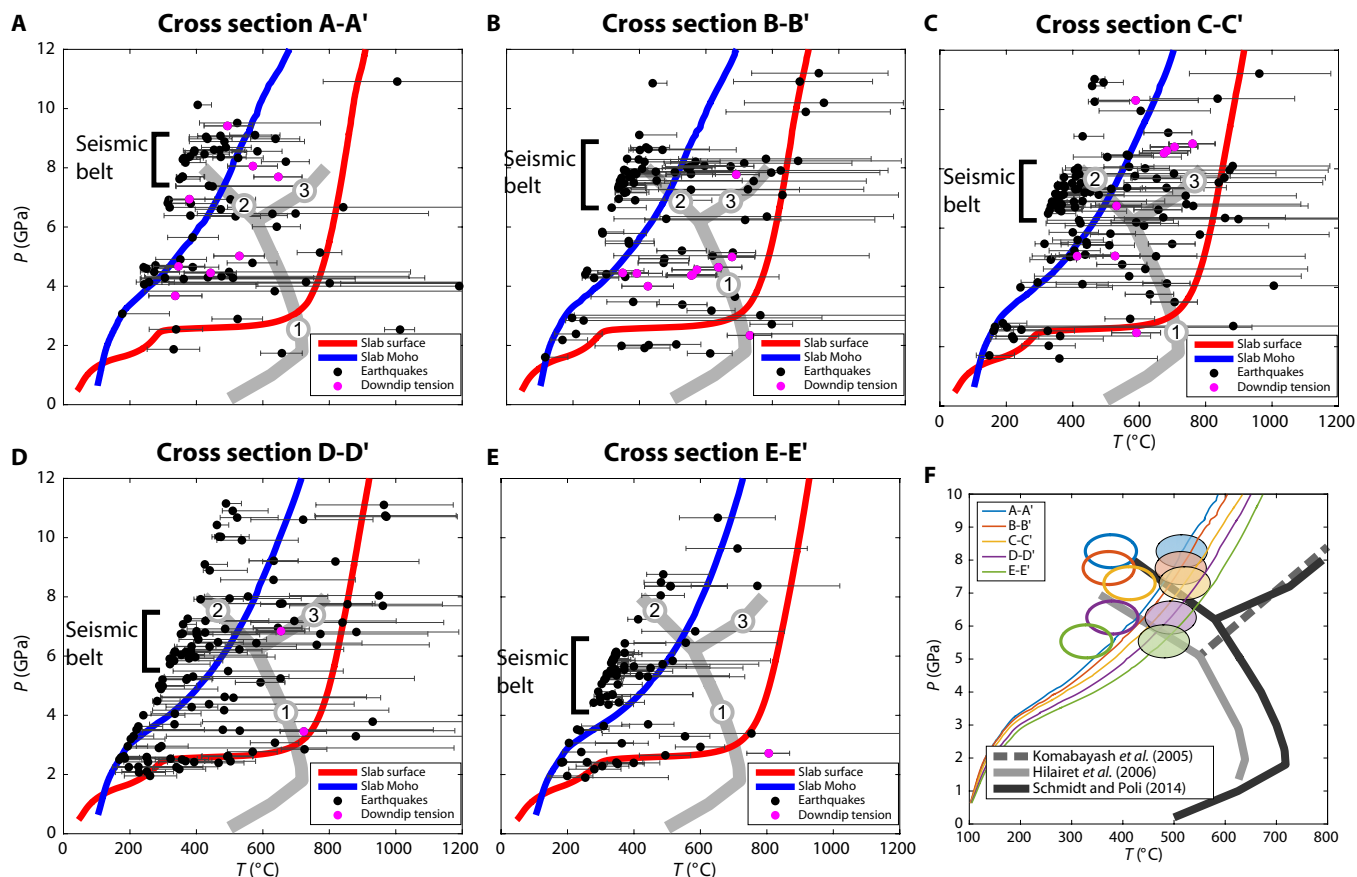


Fig. 6. Pressure-temperature conditions of earthquakes in Fig. 2. (A to E) Modeled pressures and temperatures (P - T) of earthquakes along each cross section. Black dots indicate the earthquake P - T conditions with thermal uncertainties (gray error bars). The downdip tensional events are shown in magenta. The P - T paths of the slab surface and the Moho are illustrated by the red and blue curves, respectively. Bold gray curves show the P - T conditions of the dehydration reactions (1) antigorite = forsterite + enstatite + H_2O , (2) antigorite = phase A + enstatite + H_2O , and (3) phase A = forsterite + H_2O from Schmidt and Poli (32). (F) Modeled P - T paths for the seismic belt (ellipses) and the Moho (color curves) along all cross sections. Open ellipses represent the P - T conditions of the seismic belt, whereas solid ellipses indicate the adjacent Moho P - T paths. The ellipses are quantitatively defined in figs. S9 and S10. Gray solid, gray dashed, and black solid curves show phase boundaries from studies by Komabayashi *et al.* (30), Hilairet *et al.* (31), and Schmidt and Poli (32), respectively.

We note that the experimentally determined equilibrium conditions of antigorite dehydration (30–32) show a somewhat different P - T slope than the observed nearly isothermal trends of the seismic belt and the adjacent Moho (Fig. 6F). One possible explanation is that the reaction antigorite = phase A + enstatite + H_2O may have a more isothermal trend, at pressures greater than 6 GPa, than indicated in the limited experimental data. The significant differences between the studies by Hilairet *et al.* (31) and Schmidt and Poli (32) suggest that the phase boundaries at these pressures are relatively uncertain (Fig. 6F).

An alternative explanation is that the kinetics of antigorite dehydration may effectively inhibit the reaction at temperatures lower than $\sim 450^\circ\text{C}$. In this case, the reaction would proceed near equilibrium around 5.5 GPa but would become increasingly inhibited at greater pressures, producing a nearly isothermal trend. Although the dehydration reaction antigorite = forsterite + enstatite + H_2O proceeds rapidly at temperatures above 530°C at lower pressures (38), there is no published kinetic data on the higher-pressure dehydration reaction to phase A. More detailed experimental constraints on antigorite dehydration reactions at pressures greater than 6 GPa will be required to verify the abovementioned hypotheses. Nevertheless, the nearly isothermal trend of the seismic belt, combined with the strong correlation between the maximum depths of the DSZs

and the thermal parameters for various slabs, emphasizes the predominant role of the slab temperature in dehydrating subducting mantle and triggering intermediate-depth earthquakes at these great depths.

MATERIALS AND METHODS

Locating/relocating earthquakes

Most of the data were collected from 49 ocean-bottom seismographs (OBSs) deployed in the Tonga-Lau-Fiji region from November 2009 to October 2010 and from 17 island-based seismic stations operated from October 2009 to December 2010 (red symbols in fig. S2). Each of the 29 OBSs from Woods Hole Oceanographic Institution consisted of a Guralp CMG-3T seismometer and a Quanterra Q330 datalogger, whereas the other 20 OBSs from Lamont-Doherty Earth Observatory (LDEO) used SerCEL L-4C seismometers and LDEO-designed dataloggers. The land stations were deployed on islands in Tonga and Fiji. Each of them consisted of a broadband three-component seismometer (Guralp CMG-3T, Streckeisen STS-2, or Nanometrics Trillium 120PA) and a RefTek RT130 recorder.

We first manually examined 764 earthquakes cataloged in the Reviewed International Seismological Centre (ISC) Bulletin (39) that

occurred between December 2009 and December 2010, with epicenters confined in latitudes of 16.5°S to 24°S and longitudes of 177°E to 171°W using the data from the local seismic array. *P* and *S* arrivals were manually picked, and then the events were relocated using the Antelope software with the generalized earthquake-location package (40) and the IASP91 velocity model (41). We also picked the arrivals of 399 previously unlocated earthquakes, which were automatically detected by event detection and association routines in the Antelope software, in the same region and time period but confined in a depth range of 50 to 450 km. This resulted in 94,851 *P* arrivals and 14,772 *S* arrivals for 1163 earthquakes in total. We also combined the arrival data of 292 events from the 1994 Lau Basin Ocean Bottom Seismograph Survey and the 1993–1995 Southwest Pacific Seismic Experiment (yellow symbols in fig. S2) (42, 43). To investigate the slab stress state, we also relocated earthquakes listed in the Global CMT catalog (22, 23) in the same region during 1977–2013 using the *P*, *S*, and *pP* arrivals recorded by global stations in the ISC catalog (39). *S* arrivals for epicentral distances larger than 10° were omitted because of generally large arrival time uncertainties.

Because the focus of this study is the intermediate-depth earthquakes, we used the hypocentroidal decomposition relative relocation algorithm (44, 45) to relocate only the events that were initially located within a depth range of 50 to 450 km. Including earthquakes at depths of 300 to 450 km is essential to constrain the slab geometry. The advantage of combining the local data jointly with the ISC teleseismic data in the same relative relocation is significant, because the arrivals recorded by the local stations can help to constrain the CMT events without local records through the overlapping global stations. Figure S6 shows that the relative locations of events constrained by both local and global stations are robust, independent of the inclusion of events without local records in the relocating inversion, although their absolute locations shift by ~10 km. A shift in absolute locations is expected when different station sets are used, because the different raypath coverage differently samples unknown earth heterogeneity (44, 46). However, the relative locations are robust because there are enough common stations in the station sets. The events without local records have larger location uncertainties and make the DSZ less distinct. However, these events with CMT solutions provide important information of stress state and seismic activity. We therefore primarily described the DSZ morphology on the basis of the events recorded by both local and global stations and investigated the slab stress and thermal conditions on the basis of all events.

After the initial inversion, the most poorly located events were eliminated, and the remaining data set was again relocated. This procedure was repeated several times to include only earthquakes with the smallest uncertainties. We initially divided the events into three subregions from north to south and relocated each subset. This strategy of separately locating different regions is necessary because the hypocentroidal decomposition algorithm is designed for clustered events, so that raypaths to the same station sample similar lateral heterogeneity. As some events with large uncertainties were discarded, the final round of relocation included only two subsets in the northern and southern subregions divided along 20.1°S. No significant discrepancies among hypocenters near 20.1°S were found because of this division.

A total of 671 intermediate-depth earthquakes with 95% confidence ellipsoids smaller than 8 km along all semiaxes were relocated (fig. S8). We further projected these earthquakes into five cross sections perpendicular to the Tonga Trench, each with a width of 133 km (Fig. 1 and fig. S3), and determined the slab geometry for each cross section on the basis of these events. The slab surface was fit using the smoothing spline

algorithm in MATLAB, such that the resulting surface lies above 85% of all hypocenters at depths of 50 to 400 km. The relocated hypocenters, along with their principal axes if associated with a Global CMT solution (22, 23), are plotted in figs. S3 and S4. We further sorted the events into three categories: downdip compressional events, of which *P* axes are within 30° of the slab dip vector; downdip tensional events, of which *T* axes are within 30° of the slab dip vector; and null events, which do not fall into either of the previous groupings, in many cases because the *P* or *T* axis is oriented along strike (Fig. 5).

Waveform similarity

Hypocenters of earthquakes with both local and global records show a distinct DSZ along cross section C-C'. However, because the local seismic stations were deployed for a short time period, only a few of these earthquakes have well constrained focal mechanisms. To investigate the small events without CMT solutions, we conducted an analysis of waveform similarity for earthquakes recorded by both global and local 2009–2010 stations. Figure 4A shows all events, of which only two have CMT solutions, one of which is downdip compressional and located in the upper zone and the other is downdip extensional and located in the lower zone. We compared waveforms of all the well-located 2009–2010 events recorded at station FONI, because the raypaths are roughly parallel with the slab and have similar takeoff angles. Events right beneath FONI (gray dots in Fig. 4A) were excluded to avoid near-vertical raypaths. All seismograms were filtered at a frequency of 1 to 5 Hz using a bandpass filter (fourth-order Butterworth, zero-phase shift). We then cross-correlated the waveform (± 0.4 s relative to *P* arrival) of each small event with the waveforms of the two CMT events (bold curves in Fig. 4B).

All events were then sorted into three groups according to their cross-correlation coefficients. One group shows high similarity to the downdip compressional CMT event (blue locations and waveforms in Fig. 4), and another group shows high similarity to the downdip tensional CMT event (red in Fig. 4) and events that have low or equal similarity to both events (black in Fig. 4). The histogram of depths in the slab-normal direction (Fig. 4C) suggests that the blue events concentrate near the slab surface, whereas most of the red events are 20 to 40 km deep beneath the slab surface. This analysis shows a DSZ of which the upper plane primarily consists of downdip compressional earthquakes and the lower plane contains downdip tensional events.

Modeling slab thermal structures

To investigate the *P*-*T* conditions of earthquakes in the depth range of 50 to 350 km, we developed 2D thermal models for each cross section with varying slab geometry defined in the last section. The modeling generally follows those of van Keken *et al.* (47) and Syracuse *et al.* (48), as benchmarked by van Keken *et al.* (49), in which a dynamic corner flow in the mantle wedge is driven exclusively by the kinematic motion of the slab under a fixed overriding plate. The models were calculated using a finite element approach on the basis of the SEPRAN modeling package (<http://ta.twi.tudelft.nl/sepran/sepran.html>), following the methods described by Cuvelier *et al.* (50).

By ignoring the thermal buoyancy in the wedge, secondary convection, and compressible effects of mantle, the governing equations are simplified as the conservation of mass

$$\nabla \cdot \vec{v} = 0 \quad (1)$$

and the conservation of momentum

$$\nabla \cdot \bar{\tau} - \nabla P = 0 \quad (2)$$

where \bar{v} is the velocity, P is the dynamic pressure, and $\bar{\tau}$ is the deviatoric stress tensor given by

$$\bar{\tau} = 2\eta\dot{\epsilon} \quad (3)$$

where η is the effective dynamic viscosity and $\dot{\epsilon}$ is the strain rate tensor given by

$$\dot{\epsilon}_{ij} = \frac{1}{2} \left(\frac{\partial v_i}{\partial x_j} + \frac{\partial v_j}{\partial x_i} \right) \quad (4)$$

The mantle viscosity is defined by a non-Newtonian, temperature- and stress-dependent rheology based on a dislocation creep flow law for dry olivine as

$$\eta(T, \dot{\epsilon}) = A^{-1/n} \mu \exp\left(\frac{E}{nRT}\right) \dot{\epsilon}^{(1-n)/n} \quad (5)$$

where $R = 8.3145 \text{ J mol}^{-1} \text{ K}^{-1}$ is the gas constant; A , E , μ , and n are listed in table S1 (S1). The temperature is calculated on the basis of the heat advection-diffusion equation

$$\rho c_p \left[\frac{\partial T}{\partial t} + (\bar{v} \cdot \nabla) T \right] = \nabla \cdot (\kappa \nabla T) + H \quad (6)$$

where T is the temperature, t is the time, and H is the volumetric heat production; ρ , c_p , and κ are listed in table S1. The overriding plate was modeled as a young oceanic lithosphere (half-space cooling profile) with an initial age of 10 million years (My). Thus, the modeling was time-dependent, although the kinematic descriptions and boundary conditions were fixed. We took models after evolution of 20 My, which is (more than) sufficient to reach a quasi-steady-state thermal structure.

The mantle potential temperature was assumed to be constant at 1475°C over all cross sections according to the estimation from major element chemistry at the Valu Fa Ridge (52). The condition of plate coupling between the slab and the mantle wedge is crucial for modeling the shallow part of the subduction zone. We adopted the assumption of Syracuse *et al.* (48) that the plates partially couple above 80-km depth and become fully coupled below this depth. This assumption was valid in this study because our focus was the intermediate-depth earthquakes, and the slab surface shallower than 50 km is poorly constrained because of the lack of precisely relocated seismicity.

The kinematic information of the slab for each cross section is shown in table S2, according to previous geodetic studies and modeling (27, 48, 53). The convergence rates are corrected normal to the trench, and the back-arc spreading rates are also taken into account so that V_C describes the motion of the incoming plate with respect to the arc. The other parameters, including the plate's age and sediment thickness, are set constant for all cross sections, as shown in table S2. Therefore, the differences between individual 2D thermal models come solely from the varying slab geometry and the convergence rate V_C .

Earthquake P - T conditions

The earthquake hypocenters were superposed on the 2D thermal model along each cross section, and then, the in situ pressure and temperature of the model were extracted for each event. It is worthwhile to notice that each earthquake is treated as a point source near the initial nucleation, although large earthquake ruptures should extend widely in space and thus broadly in the P - T diagram. Given the strong thermal gradients near the slab surface, relatively small errors in hypocenter location can translate into large differences in predicted temperature. We thus estimated the uncertainties of the slab location to be ~ 5 km normal to the slab and further calculated the corresponding uncertainties of temperature and pressure for the earthquakes. The estimated errors of pressure were negligible, but the thermal uncertainties were as large as 300°C for earthquakes near the slab surface (Fig. 6, A to E).

To precisely locate the seismic belt in the P - T diagrams, we plotted histograms of pressures and temperatures of earthquakes (fig. S9). The seismic belt was identified as the peak of the distribution. The Moho temperature adjacent to a hypocenter was obtained by shifting the temperature to the Moho path in the P - T diagrams while keeping the pressure unchanged. This strategy was based on the fact that the thermal gradient is much larger than the pressure gradient. Therefore, the P - T condition of the Moho adjacent to the seismic belt was defined as the peak of seismic activity in both pressure and shifted temperature (fig. S10). Although the pressure of the seismic belt consistently decreases from north to south, its temperature is restricted in a narrow range of 325° to 425°C. In addition, the temperature of the Moho adjacent to the seismic belt is confined in an even narrower range of 475° to 525°C.

SUPPLEMENTARY MATERIALS

Supplementary material for this article is available at <http://advances.sciencemag.org/cgi/content/full/3/1/e1601755/DC1>

fig. S1. Cross sections of hypocenters.

fig. S2. Tectonic map and seismic stations.

fig. S3. Map view of relocated Global CMT solutions.

fig. S4. Cross sections of earthquake at vertical depths of 50 to 300 km with Global CMT solutions.

fig. S5. Cross sections of earthquake principal axes based on Global CMT solutions.

fig. S6. Cross sections of hypocenters from different inversions.

fig. S7. Histograms of earthquake depths along each cross section.

fig. S8. 3D view of error ellipses for all events, viewed normal to the trench.

fig. S9. Histograms of earthquake P - T conditions along each cross section.

fig. S10. Histograms of P - T conditions of the Moho adjacent to the seismic belt along each cross section.

table S1. Thermodynamic parameters used in thermal modeling.

table S2. Slab parameters for each cross section.

References (54)

REFERENCES AND NOTES

1. N. Umino, A. Hasegawa, On the two-layered structure of deep seismic plane in northeastern Japan arc. *J. Seismol. Soc. Jpn.* **27**, 125–139 (1975).
2. H. Kawakatsu, Double seismic zone in Tonga. *Nature* **316**, 53–55 (1985).
3. E. R. Engdahl, C. H. Scholz, A double Benioff zone beneath the central Aleutians: An unbending of the lithosphere. *Geophys. Res. Lett.* **4**, 473–476 (1977).
4. K. W. Hudnut, J. J. Taber, Transition from double to single Wadati-Benioff seismic zone in the Shumagin Islands, Alaska. *Geophys. Res. Lett.* **14**, 143–146 (1987).
5. J. J. McGuire, D. A. Wiens, A double seismic zone in New Britain and the morphology of the Solomon Plate at intermediate depths. *Geophys. Res. Lett.* **22**, 1965–1968 (1995).
6. H. Kao, R.-J. Rau, Detailed structures of the subducted Philippine Sea Plate beneath northeast Taiwan: A new type of double seismic zone. *J. Geophys. Res.* **104**, 1015–1033 (1999).
7. A. Rietbrock, F. Waldhauser, A narrowly spaced double-seismic zone in the subducting Nazca plate. *Geophys. Res. Lett.* **31**, L10608 (2004).
8. S. Kita, T. Okada, A. Hasegawa, J. Nakajima, T. Matsuzawa, Existence of interplane earthquakes and neutral stress boundary between the upper and lower planes of the

- double seismic zone beneath Tohoku and Hokkaido, northeastern Japan. *Tectonophysics* **496**, 68–82 (2010).
9. H. Shiohara, H. Sugioka, K. Mochizuki, S. Oki, T. Kanazawa, Y. Fukao, K. Suyehiro, Double seismic zone in the North Mariana region revealed by long-term ocean bottom array observation. *Geophys. J. Int.* **183**, 1455–1469 (2010).
 10. M. R. Brudzinski, C. H. Thurber, B. R. Hacker, E. R. Engdahl, Global prevalence of double Benioff zones. *Science* **316**, 1472–1474 (2007).
 11. S. Kirby, E. R. Engdahl, R. Denlinger, in *Subduction Top to Bottom*, G. E. Bebout, D. W. Scholl, S. H. Kirby, J. P. Platt, Eds. (American Geophysical Union, 1996), pp. 195–214.
 12. B. E. Hobbs, A. Ord, Plastic instabilities: Implications for the origin of intermediate and deep focus earthquakes. *J. Geophys. Res.* **93**, 10521–10540 (1988).
 13. P. E. van Keken, S. Kita, J. Nakajima, Thermal structure and intermediate-depth seismicity in the Tohoku-Hokkaido subduction zones. *Solid Earth* **3**, 355–364 (2012).
 14. S. M. Peacock, Are the lower planes of double seismic zones caused by serpentine dehydration in subducting oceanic mantle? *Geology* **29**, 299–302 (2001).
 15. B. R. Hacker, S. M. Peacock, G. A. Abers, S. D. Holloway, Subduction factory 2—Are intermediate-depth earthquakes in subducting slabs linked to metamorphic dehydration reactions? *J. Geophys. Res.* **108**, B12030 (2003).
 16. T. Yamasaki, T. Seno, Double seismic zone and dehydration embrittlement of the subducting slab. *J. Geophys. Res.* **108**, 2212 (2003).
 17. M. Faccenda, T. V. Gerya, N. S. Mancktelow, L. Moresi, Fluid flow during slab unbending and dehydration: Implications for intermediate-depth seismicity, slab weakening and deep water recycling. *Geochem. Geophys. Geosyst.* **13**, Q01010 (2012).
 18. M. Bevis, F. W. Taylor, B. E. Schutz, J. Recy, B. L. Isacks, S. Helu, R. Singh, E. Kendrick, J. Stowell, B. Taylor, S. Calmantli, Geodetic observations of very rapid convergence and back-arc extension at the Tonga arc. *Nature* **374**, 249–251 (1995).
 19. B. Isacks, P. Molnar, Distribution of stresses in the descending lithosphere from a global survey of focal-mechanism solutions of mantle earthquakes. *Rev. Geophys.* **9**, 103–174 (1971).
 20. H. Kawakatsu, Downdip tensional earthquakes beneath the Tonga Arc: A double seismic zone? *J. Geophys. Res.* **91**, 6432–6440 (1986).
 21. International Seismological Centre (ISC), *EHB Bulletin* (ISC, 2009); www.isc.ac.uk/ehbulletin.
 22. A. M. Dziewoński, T.-A. Chou, J. H. Woodhouse, Determination of earthquake source parameters from waveform data for studies of global and regional seismicity. *J. Geophys. Res.* **86**, 2825–2852 (1981).
 23. G. Ekström, M. Nettles, A. M. Dziewoński, The global CMT project 2004–2010: Centroid-moment tensors for 13,017 earthquakes. *Phys. Earth Planet. Inter.* **200–201**, 1–9 (2012).
 24. D. H. Christensen, T. Lay, Large earthquakes in the Tonga region associated with subduction of the Louisville Ridge. *J. Geophys. Res.* **93**, 13367–13389 (1988).
 25. C. Cai, D. A. Wiens, Dynamic triggering of deep earthquakes within a fossil slab. *Geophys. Res. Lett.* **43**, 9492–9499 (2016).
 26. T. Seno, Y. Yamanaka, Arc stresses determined by slabs: Implications for mechanisms of back-arc spreading. *Geophys. Res. Lett.* **25**, 3227–3230 (1998).
 27. E. M. Syracuse, G. A. Abers, Global compilation of variations in slab depth beneath arc volcanoes and implications. *Geochem. Geophys. Geosyst.* **7**, Q05017 (2006).
 28. S. Kita, T. Okada, A. Hasegawa, J. Nakajima, T. Matsuzawa, Anomalous deepening of a seismic belt in the upper-plane of the double seismic zone in the Pacific slab beneath the Hokkaido corner: Possible evidence for thermal shielding caused by subducted forearc crust materials. *Earth Planet. Sci. Lett.* **290**, 415–426 (2010).
 29. W. C. Crawford, J. A. Hildebrand, L. M. Dorman, S. C. Webb, D. A. Wiens, Tonga Ridge and Lau Basin crustal structure from seismic refraction data. *J. Geophys. Res.* **108**, 2195 (2003).
 30. T. Komabayashi, K. Hirose, K.-i. Funakoshi, N. Takafuji, Stability of phase A in antigorite (serpentine) composition determined by in situ x-ray pressure observations. *Phys. Earth Planet. Inter.* **151**, 276–289 (2005).
 31. N. Hilaret, I. Daniel, B. Reynard, Equation of state of antigorite, stability field of serpentines, and seismicity in subduction zones. *Geophys. Res. Lett.* **33**, L02302 (2006).
 32. M. W. Schmidt, S. Poli, in *Treatise on Geochemistry*, vol. 4, The Crust, H. D. Holland, K. K. Turekian, Eds. (Elsevier, ed. 2, 2014), pp. 669–701.
 33. C. R. Ranero, J. P. Morgan, K. McIntosh, C. Reichert, Bending-related faulting and mantle serpentinization at the Middle America trench. *Nature* **425**, 367–373 (2003).
 34. H. J. A. van Avendonk, W. S. Holbrook, D. Lizarralde, P. Denyer, Structure and serpentinization of the subducting Cocos plate offshore Nicaragua and Costa Rica. *Geochem. Geophys. Geosyst.* **12**, Q06009 (2011).
 35. E. Contreras-Reyes, I. Grevemeyer, A. B. Watts, E. R. Flueh, C. Peirce, S. Moeller, C. Papenberg, Deep seismic structure of the Tonga subduction zone: Implications for mantle hydration, tectonic erosion, and arc magmatism. *J. Geophys. Res.* **116**, 10.1029/2011JB008434 (2011).
 36. D. J. Shillington, A. Bécel, M. R. Nedimović, H. Kuehn, S. C. Webb, G. A. Abers, K. M. Keranen, J. Li, M. Delescluse, G. A. Mattei-Salicip, Link between plate fabric, hydration and subduction zone seismicity in Alaska. *Nat. Geosci.* **8**, 961–964 (2015).
 37. C. R. Wilson, M. Spiegelman, P. E. van Keken, B. R. Hacker, Fluid flow in subduction zones: The role of solid rheology and compaction pressure. *Earth Planet. Sci. Lett.* **401**, 261–274 (2014).
 38. J.-P. Perrillat, I. Daniel, K. T. Koga, B. Reynard, H. Cardon, W. A. Crichton, Kinetics of antigorite dehydration: A real-time x-ray diffraction study. *Earth Planet. Sci. Lett.* **236**, 899–913 (2005).
 39. International Seismological Centre (ISC), *Reviewed ISC Bulletin* (ISC, 2013); www.isc.ac.uk/iscbulletin/review/.
 40. G. L. Pavlis, F. Vernon, D. Harvey, D. Quinlan, The generalized earthquake-location (GENLOC) package: An earthquake-location library. *Comput. Geosci.* **30**, 1079–1091 (2004).
 41. B. L. N. Kennett, E. R. Engdahl, Traveltimes for global earthquake location and phase identification. *Geophys. J. Int.* **105**, 429–465 (1991).
 42. K. D. Koper, D. A. Wiens, L. M. Dorman, J. A. Hildebrand, S. C. Webb, Modeling the Tonga slab: Can travel time data resolve a metastable olivine wedge? *J. Geophys. Res.* **103**, 30079–30100 (1998).
 43. D. A. Wiens, H. J. Gilbert, B. Hicks, M. E. Wyssession, P. J. Shore, Aftershock sequences of moderate-sized intermediate and deep earthquakes in the Tonga Subduction Zone. *Geophys. Res. Lett.* **24**, 2059–2062 (1997).
 44. T. H. Jordan, K. A. Sverdrup, Teleseismic location techniques and their application to earthquake clusters in the South-Central Pacific. *Bull. Seismol. Soc. Am.* **71**, 1105–1130 (1981).
 45. E. A. Bergman, S. C. Solomon, Earthquake swarms on the Mid-Atlantic Ridge: Products of magmatism or extensional tectonics? *J. Geophys. Res.* **95**, 4943–4965 (1990).
 46. C. J. Wolfe, On the mathematics of using difference operators to relocate earthquakes. *Bull. Seismol. Soc. Am.* **92**, 2879–2892 (2002).
 47. P. E. van Keken, B. Kiefer, S. M. Peacock, High-resolution models of subduction zones: Implications for mineral dehydration reactions and the transport of water into the deep mantle. *Geochem. Geophys. Geosyst.* **3**, 1056 (2002).
 48. E. M. Syracuse, P. E. van Keken, G. A. Abers, The global range of subduction zone thermal models. *Phys. Earth Planet. Inter.* **183**, 73–90 (2010).
 49. P. E. van Keken, C. Currie, S. D. King, M. D. Behn, A. Cagnioncle, J. He, R. F. Katz, S.-C. Lin, E. Marc Parmentier, M. Spiegelman, K. Wang, A community benchmark for subduction zone modeling. *Phys. Earth Planet. Inter.* **171**, 187–197 (2008).
 50. C. Cuvelier, A. Segal, A. A. van Steenhoven, *Finite Element Methods and Navier-Stokes Equations* (Mathematics and Its Applications, D. Reidel Publishing Company, 1986), 504 pp.
 51. S.-i. Karato, P. Wu, Rheology of the upper mantle: A synthesis. *Science* **260**, 771–778 (1993).
 52. S. S. Wei, D. A. Wiens, Y. Zha, T. Plank, S. C. Webb, D. K. Blackman, R. A. Dunn, J. A. Conder, Seismic evidence of effects of water on melt transport in the Lau back-arc mantle. *Nature* **518**, 395–398 (2015).
 53. K. E. Zellmer, B. Taylor, A three-plate kinematic model for Lau Basin opening. *Geochem. Geophys. Geosyst.* **2**, 10.1029/2000GC000106 (2001).
 54. G. P. Hayes, D. J. Wald, R. L. Johnson, Slab1.0: A three-dimensional model of global subduction zone geometries. *J. Geophys. Res.* **117**, B01302 (2012).

Acknowledgments: We thank H. Fisher, H. Jasperson, and A. Adams for helping with data processing and B. R. Hacker, W. Fan, P. M. Shearer, and X. Yue for constructive discussions. Three anonymous reviewers provided thoughtful comments that greatly improved this manuscript. We thank P. J. Shore, D. Heeszel, E. Emry, L. Vuetibau, T. Fatai, Fiji Department of Mineral Resources, and Tonga Ministry of Lands, Survey, and Natural Resources, as well as the captains and crew of the *R/Vs Revelle* and *Kilo Moana* for assistance with data collection. The Portable Array Seismic Studies of the Continental Lithosphere (PASSCAL) program of the Incorporated Research Institutions in Seismology (IRIS), and the Ocean Bottom Seismograph Instrument Pool facilities at Woods Hole Oceanographic Institution and Lamont-Doherty Earth Observatory provided seismic instrumentation for this project. **Funding:** This work was made possible by funding from NSF grants OCE-0426408 and EAR-0911137 to D.A.W. and OCE-1249353 and OCE-1356132 to P.E.v.K. S.S.W. was supported by the McDonnell International Scholars Academy and the Cecil H. and Ida M. Green Foundation. **Author contributions:** S.S.W. and C.C., advised by D.A.W., analyzed the seismic data. P.E.v.K. developed the thermal models. S.S.W. took the lead in writing the manuscript, and all authors discussed the results and edited the manuscript. **Competing interests:** The authors declare that they have no competing interests. **Data and materials availability:** All data needed to evaluate the conclusions in the paper are present in the paper and/or the Supplementary Materials. Additional data related to this paper may be requested from the authors. Raw seismic data are available at the IRIS Data Management Center (www.iris.edu/dms/nodes/dmc).

Submitted 28 July 2016
 Accepted 29 November 2016
 Published 11 January 2017
 10.1126/sciadv.1601755

Citation: S. S. Wei, D. A. Wiens, P. E. van Keken, C. Cai, Slab temperature controls on the Tonga double seismic zone and slab mantle dehydration. *Sci. Adv.* **3**, e1601755 (2017).

Slab temperature controls on the Tonga double seismic zone and slab mantle dehydration

S. Shawn Wei, Douglas A. Wiens, Peter E. van Keken and Chen Cai

Sci Adv **3** (1), e1601755.

DOI: 10.1126/sciadv.1601755

ARTICLE TOOLS

<http://advances.sciencemag.org/content/3/1/e1601755>

SUPPLEMENTARY MATERIALS

<http://advances.sciencemag.org/content/suppl/2017/01/09/3.1.e1601755.DC1>

REFERENCES

This article cites 47 articles, 5 of which you can access for free
<http://advances.sciencemag.org/content/3/1/e1601755#BIBL>

PERMISSIONS

<http://www.sciencemag.org/help/reprints-and-permissions>

Use of this article is subject to the [Terms of Service](#)

Science Advances (ISSN 2375-2548) is published by the American Association for the Advancement of Science, 1200 New York Avenue NW, Washington, DC 20005. The title *Science Advances* is a registered trademark of AAAS.

Copyright © 2017, The Authors